Geometry-based structural form-finding to design architected cellular solids

Mostafa Akbari*
akbariae@design.upenn.edu
Polyhedral Structures Laboratory, Weitzman School of
Design, University of Pennsylvania,
Philadelphia, Pennsylvania, USA

Armin Mirabolghasemi
AM3L, Department of Bioresource Engineering McGill
University
Montreal, Quebec, Canada

Hamid Akbarzadeh
AM3L, Department of Bioresource Engineering McGill
University
Montreal, Quebec, Canada

Masoud Akbarzadeh
Polyhedral Structures Laboratory, Weitzman School of
Design, University of Pennsylvania
Philadelphia, Pennsylvania, USA
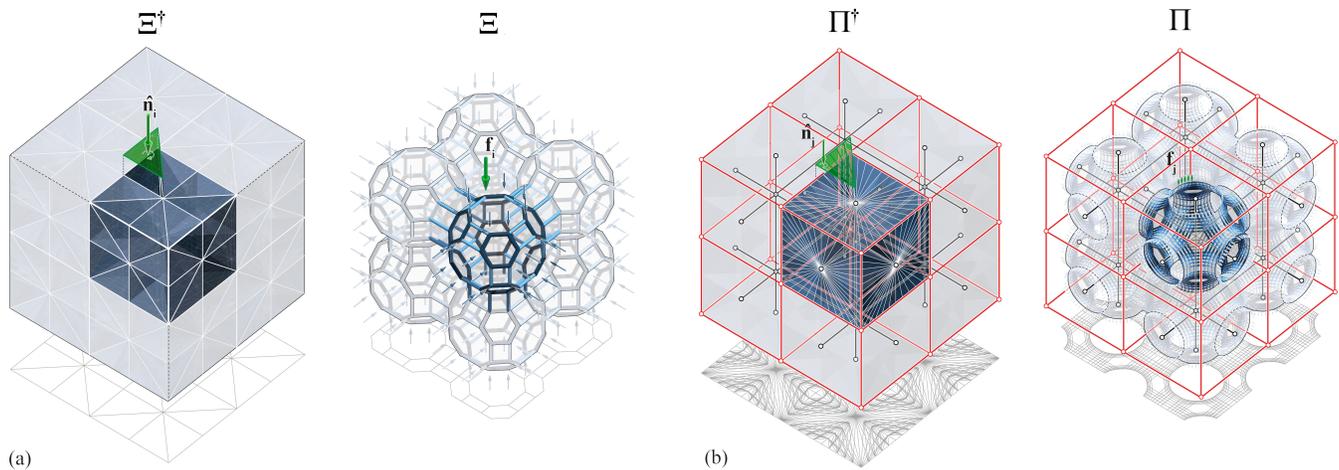
Figure 1: (a) Aggregation of the force and form diagrams of a truss cellular unit-cell and (b) aggregation of the force and form diagrams of a shell-based cellular (shellular) unit-cell (similar to the Schwarz P unit-cell) generated in 3DGS.

ABSTRACT

In this paper, we introduce a geometry-based structural design method as an alternative approach for designing low-density structures applicable to material science and mechanical engineering. This method will provide control over internal force-flow, boundary condition, and applied loads. The methodology starts with an introduction to the principles of geometric equilibrium and continues by introducing multiple design techniques to generate truss cellular, polyhedron cellular, and shell cellular (or Shellular) materials by manipulating the geometry of the equilibrium of force. The research concludes by evaluating the mechanical performance of a range of cellular structures designed by this approach.

KEYWORDS

cellular structures, Shellulars, graphic statics, structural form-finding, geometry-based equilibrium

1 INTRODUCTION

1.1 Architecture of low-density materials

Cellular materials are light-weight and porous materials with tunable multi-functional properties. They can have a variety of applications where high load-bearing capacity with a very low density is desired [Christensen 1986; Eynbeygui et al. 2020; Shi and Akbarzadeh 2019]. In the literature, the taxonomy of cellular materials,

based on the geometric configuration of each unit cell, includes truss cellular, polyhedron cellular, and shell cellular (or shellular) materials (Figure 2) [Gibson and Ashby 1999; Han et al. 2015a; Savio et al. 2018]. These unit cells can either be tessellated in periodic or stochastic shapes. Each cell's shape and connectivity to the others in a periodic cellular material are prescribed uniformly, such as the regular hexagon honeycomb pattern. While the shape of a stochastic cellular material emerges as a result of an underlying stochastic function such as Voronoi patterns [Bhate et al. 2019].

1.1.1 Truss cellular materials. The architecture of these structures comprises a network of slender members similar to the skeleton of a glass sponge in nature (Figure 2a). Topologically speaking, we can describe these materials' geometry as a group of vertices v_i and edges e_i, where each vertex is connected to two or more edges. The number of edges each vertex is connected to is called the *degree* or *valence* of the vertex. For periodic truss cellular materials, each unit cell's geometry and topology, such as the valence of each vertex in different cells, is consistent, while in the stochastic version, they might be different [Bhate et al. 2019].

The mechanical properties of periodic truss cellular materials linearly decreases as the relative density (ρ) reduces, while in stochastic cellular materials decrease more rapidly (i.e. proportionally to $(\rho/\rho_s)^2 = (\rho/\rho_s)^3$) [Gibson and Ashby 1999; Ma et al. 2001]. Cellular materials can deform under external loading by either bending or stretching of the cell members. Stretching-dominated materials are much more weight-efficient for structural applications [Deshpande et al. 2001]. When periodic truss cellular materials are subjected to external loading, axial force as tension or compression act along each strut member, resulting in high strength and stiffness. Compared to stochastic cellular materials with bending-dominated deformation, periodic truss cellular materials' deformation is stretching-dominated [Han et al. 2015a; Ma et al. 2001].

Abrupt geometric change near the connections of truss cellular systems causes stress concentration [Torrents et al. 2012], which may increase the flaws of fabrication and affect the mechanical performance of the material. Besides, the structural performance of these materials (in compression) relies on the buckling performance of the members [Akbari et al. 2019; Meza et al. 2014].

1.1.2 polyhedron cellular materials. The architecture of these materials composed of closed cells with membranes similar to club moss in nature (Figure 2b). Topologically, these materials consist of a group of cells c_i, faces f_i, edges e_i, and vertices v_i. Each edge in this typology is connected to more than two faces, called singular or a non-manifold edge [Bloomenthal and Ferguson 1995].

The Mechanical performance of the structure is proportional to its relative density (measured density, ρ, divided by the density of the constituent solid, ρ_s). Concerning other cellular materials, closed polyhedrons take much material, which makes it challenging to produce at low-density. Besides, since there is no access to the cells' internal space to transfer material, closed cells limit their applications that require material transformation inside the cells, except for thermal insulation [Gibson and Ashby 1999; Han et al. 2015a].

1.1.3 Shell cellular materials (Shellulars). The third possible option to achieve ultra-low density materials is shell cellular materials or Shellulars. Shellulars are stretching-dominated materials with simpler architecture than truss cellular materials [Han et al. 2015a]. This typology consists of a group of unit cells, faces f_i, edges e_i, and vertices v_i. In this typology, compared to polyhedron cellular materials, each edge e_i is adjacent to only two faces, called a regular or a two-manifold edge [Bloomenthal and Ferguson 1995]. That is why these materials do not have self-intersections. A group of these unit cells results in a single continuous smooth-curved shell. In nature, we can find similar geometries on the surfaces of Urchin plates (Figure 2c) [Han et al. 2015a]. A typical example of these surfaces is the triply periodic minimal surface (TPMS), which was described by H. A. Schwarz in the 19th century [Hyde et al. 1996].

Minimal surfaces are intersection-free smooth surfaces that have zero mean curvature at every point on the surface ($H = (k_1+k_2)/2 = 0$, k_1 and k_2 are the principal curvatures of the surface at each point). They are surfaces with the minimum area between given boundary conditions resulting in the least amount of material and weight (as observed in soap films formed in rigid frames [Hyde et al. 1996]). The crystalline structure of minimal surfaces allows them to repeat in three dimensions, resulting in triply periodic minimal surfaces(TPMS) [Hyde et al. 1996]. If a thin shell takes the form of a minimal surface, it will demonstrate significant resistance under external loads, showing the uniform distribution of the stresses in the shell [Rajagopalan and Robb 2006a]. Recent studies show that the high surface-to-volume ratio of TPMSs enhances the mechanical performance of the system [Han et al. 2017]. In small scales, the TPMSs, such as Gyroid, Schwarz P, or Schwarz W are used as space-filling, rigid micro-structures to produce light-weight and high-performance materials [Han et al. 2015b; Qin et al. 2017].

1.2 Geometric modeling of cellular architectures

Geometric modeling of low-density structures can be classified into two main groups, Implicit and explicit modeling [Rajagopalan and Robb 2006b]. Implicit modeling is a way to model geometry using mathematical equations. For instance, for designing a shellular material, we would be able to model a *continuous* surface using a single-valued function of three variables. The resulted surface is the positions of points for which the function has a constant value.

While with this method, one can model the geometry of a shellular material with a high degree of precision, lack of topology information (in order to describe the surface as a discrete system including faces, edges, and vertices) restricts its application. In order to explicitly model a cellular geometry, we need to iteratively refine an initial geometry defined by its boundary [Rajagopalan and Robb 2006b]. First, we need to model a simplified version of the geometry as a curve skeleton [Thiery et al. 2012] (e.g., for modeling a truss cellular geometry) or a pin-jointed net (e.g., for modeling a shellular geometry). Then, in order to visualize the existing network, we may either use a boundary representation technique (B-rep) or a volume representation technique (V-rep) [Savio et al. 2018]. The B-rep method represents a geometry using boundary limits, and the v-rep method (or solid modeling) represents a complex solid as a boolean operator (e.g., union) of elementary geometries [Savio et al. 2018].
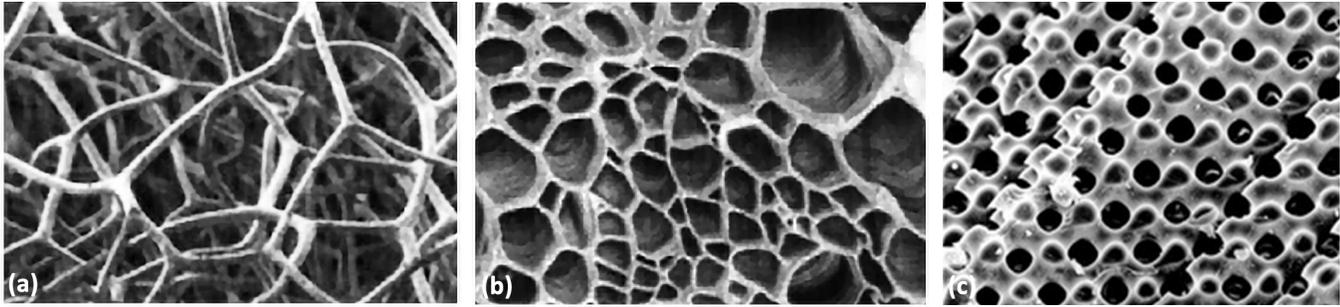
Figure 2: Cellular materials in nature; (a) Sponge (an example of truss cellular material); (b) Iris leaf (an instance of polyhedron cellular material) [Gibson and Ashby 1999]; (c) cross-section through a sea urchin skeletal plate (showing resemblance to Schwarz P surface, an example of shell cellular (shellular) material) [Lai et al. 2007].
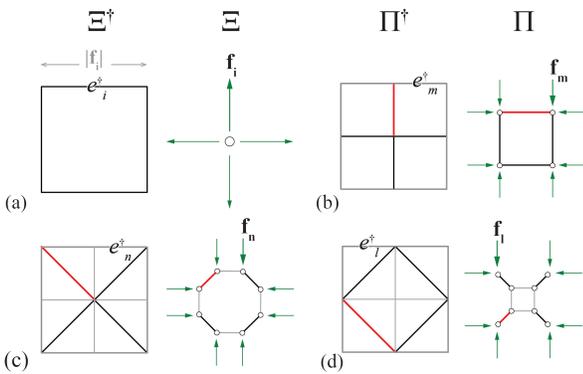
Figure 3: (a) Force and form diagram of a node in equilibrium in 2DGS; (b) internal subdivision of the force diagram results in a frame (2d cell) in equilibrium as a form diagram; (c),(d) additional subdivision of the force diagram without changing the external edges results in different 2d structures in equilibrium.

1.3 Structural modeling of cellular architectures

The modeling methods represented in section 1.2 only address the pure geometric configuration of material without considering the force distribution in the system. *Structural* modeling methods such as structural form-finding and topology optimization consist of various techniques to find efficient structural forms for discrete networks. [Goldsmith 2016; Sigmund and Maute 2013] Structural form-finding techniques fall into the following categories; physical, numerical, and geometric form-finding methods. In the physical form-finding method, the designer needs to build a physical model to evaluate its structural performance through material behavior. Each design iteration in this method requires building a new model, which is a time-consuming process [Goldsmith 2016]. Numerical methods were developed to avoid the problems of physical form-finding techniques. These methods simulate the behavior of the material subjected to the force. One of the well-known numerical methods is the force-density, which is based on the force-length ratios defined for each branch of a net structure [Adriaenssens et al.

2014; Pinkall and Polthier 1993; Schling et al. 2017; Veenendaal and Block 2012]. These methods work like a black box and will not let the designer understand or see the effective parameters in the design process [Akbarzadeh 2016].

Finite element-based optimization, as an example of topology optimization techniques, optimizes material layout within a given design space using the finite element method(FEM). This method receives a volume as an input, and after analyzing the stress distribution for a given external loading scenario, it tries to optimize the material using Boolean subtraction. The boolean operation, rendering, and visualization in this technique requires significant computational resources and large physical memory. Besides, this method always works with the form without knowing the system's force in the design process and does not control the structure's geometry and topology. [Bendsoe and Kikuchi 1988; Huang et al. 2013; Requicha and Voelcker 1977; Sigmund and Maute 2013]

1.4 Geometry-based structural form-finding

As the third category of structural form-finding methods, the geometric form-finding method is an intuitive structural modeling technique, describing the equilibrium of a structure using visual geometric relations [Veenendaal and Block 2012]. In this method, geometrical representation has been used to show the equilibrium of the forces in a structure. Graphic statics, as a geometry-based structural form-finding technique, is a powerful method for designing and analyzing complex structures in 2D and 3D [Cremona 1890; Culmann 1864; Maxwell 1864; Rankine 1864; Van Mele et al. 2012; Wolfe 1921]. This method started by M. Rankine and J. Maxwell in the 19th century [Maxwell 1864; Rankine 1864] but continues to be used and developed even today [Akbarzadeh 2016; Block 2009]. Graphic statics lets us understand the force-flow while designing the structure. With this method, we can design various structures with different topology while we have control over their form and force. This technique generates axially loaded structures in equilibrium in which no bending occurs [Akbarzadeh et al. 2015a]. The strength of this method lies in the clear relation between *form and force diagrams* as a pair of reciprocal diagrams linked through simple geometric constrains (Figure 3 and 4). The *form diagram* represents the structure's geometry combined with reaction forces and applied loads, and the *force diagram* represents the equilibrium

of forces acting on and in the structure. The closeness of the force polygon (in 2d graphic statics) and force polyhedron (in 3d graphic statics) tells us that the structure is in equilibrium [Akbarzadeh et al. 2016; Maxwell 1864; Rankine 1864].

1.4.1 2D Graphic statics (2DGS).

The geometry and topology of reciprocal diagrams in 2DGS. If we consider a system of co-planar intersecting bars in the plan PL_m as a rope with four segments being pulled from all sides (force diagrams have been marked by Greek letters with † sign) (Figure 3a, Ξ), to find the magnitude of forces in each segment (e.g. $|f_i|$), it is enough to construct the polygon of force or the *force diagram* (Figure 3a, $\Xi^\dagger$). Each edge (e.g. $e_i^\dagger$) of force diagram is perpendicular to the direction of each segment (f_i) in the bars system or *form diagram* (Figure 3a, Ξ) [Maxwell 1864; Rankine 1864]. Closeness of the force polygon tells us that the ropes are in equilibrium [Akbarzadeh et al. 2016]. Moreover, the length of each edge (e.g. $e_i^\dagger$) of the force diagram (Figure 3a, $\Xi^\dagger$) represents the magnitude of the force ($|f_i|$) in the reciprocal rope in the form diagram (Figure 3a, Ξ) [Maxwell 1864; Rankine 1864]. The force polygon as a force diagram corresponds to a node in equilibrium in 2d as a form diagram. The edges of the force diagram are perpendicular to the members of the form diagram (edges and reaction forces) [Maxwell 1864; Rankine 1864].

Effect of subdivision of the force diagram on the topology of the form diagram in 2DGS. In Figure 3b, $\Pi^\dagger$, Internal subdivision of the force polygon from a square to four squares results in a 2d cell in equilibrium as a form diagram (Figure 3b, Π) [Van Mele et al. 2012]. Additional subdivision of the force diagram without changing the external edges results in more detailed structures in equilibrium with the same external loads (Figure 3a). The bidirectional relation between the force and form diagram throughout the design process helps the designer intuitively understand the system's behavior.

1.4.2 3D Graphic statics (3DGS).

The geometry of the reciprocal diagrams in 3DGS. If a polygon represents the equilibrium of a node in 2D (as a force diagram), a closed polyhedron in 3D can represent the equilibrium of a three-dimensional node (Figure 4a, $\Xi^\dagger$). According to the "Divergence theorem" and the principles of graphic statics [Culmann 1864; do Carmo 1976; Katz 1979; Wolfe 1921], If the forces (f_i) applied to a node in space (Figure 4a, Ξ) are perpendicular to the faces ($f_i^\dagger$) of a closed polyhedron, the sum of these forces must be zero, leaving the node in equilibrium. The node and applied forces represent the *form diagram* (Figure 4a, Ξ) in 3d, while the closed polyhedron represents the *force diagram* (Figure 4a, $\Xi^\dagger$). The magnitude of the forces ($|f_i|$) in the form diagram is proportional to the areas of the faces (A_{f_i}) in the force diagram [Akbarzadeh 2016; Akbarzadeh et al. 2015b]. Therefore, in order to represent the force-flow in the form diagram, we can visualize the force distribution via adding thickness to each member of the form diagram proportional to the corresponding faces in the force diagram (Figure 4).

The topology of the reciprocal diagrams in 3DGS. Topologically, reciprocal polyhedral diagrams (form and force diagrams in 3d) consist of vertices, edges, faces, and cells. These two diagrams are

(a)

(b)

(c)

(d)

(e)

(f)

(g)

(h) $A(f_j) = |f_i|$

$|f_i| = 2 \times |f_{i,1}| = 4 \times |f_{i,2}| = 8 \times |f_{i,3}|$
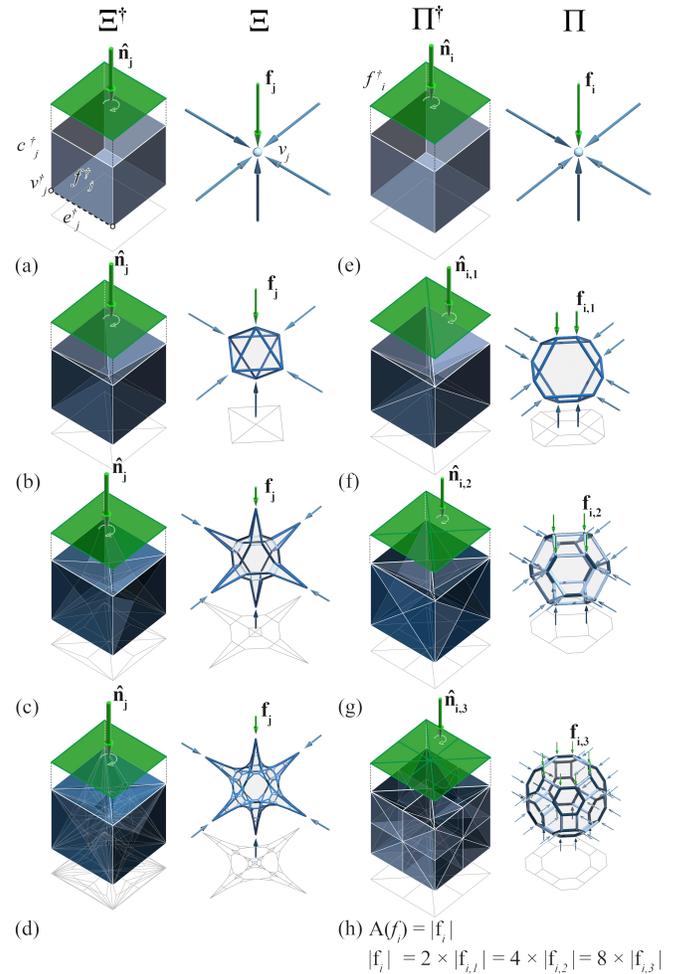
Figure 4: Different types of force diagram's subdivisions in 3d result in new form diagrams; (a),(e) a closed cube as a force diagram represents a node in equilibrium; (a-d) internal subdivision of a force diagram without subdividing the global faces; (e-h) subdivision of a force diagram while subdividing the external faces and extruding inside.

reciprocal and they have certain characteristics as mentioned bellow (Figure 4) [Akbarzadeh et al. 2015b];

- they are *dual*, which means each edge, vertex, cell, and face in the form diagram (e_i, v_i, c_i, f_i) (Figure 4a, $\Xi^\dagger$), respectively, corresponds to one and only one face, cell, vertex, and edge ($f_i^\dagger, c_i^\dagger, v_i^\dagger, e_i^\dagger$) (Figure 4a, Ξ);
- all faces are planar and all edges are perpendicular to their dual faces;
- the direction of force $\mathbf{f}_j$ in the form diagram is as same as the normal $\mathbf{n}_j$ in the force diagram; and
- a system of forces is in pure tension or compression if their force polyhedron is convex and is a proper cell decomposition of space (when every point in space belongs to one cell

at least, the cells have disjoint interiors, and every face of one cell is a complete face of another cell).

In reciprocal diagrams (Figure 4a), each cell $c_j^\dagger$ in the force diagram (force diagram's topology have been marked by italic letters with † sign) corresponds to a single node v_j in the form diagram. In addition, face $f_j^\dagger$, edge $e_j^\dagger$, and vertex $v_j^\dagger$ in the force diagram correspond to edge e_j, face f_j, and vertex v_j in the form diagram (in order to simplifying the figure, the form diagrams have been shown as pin-jointed structures and form diagrams' cells and faces have not been shown).

1.5 Problem statement and objectives

Some of these techniques, like mathematical-based methods, are mostly based on complex equations, and lack of topology information may restrict their applications in computer-aided geometric design. [Rajagopalan and Robb 2006b] Tuning topological elements let us design new geometries or deform the existing ones to the desired shape. Moreover, designing cellular materials using any arbitrary geometric configuration does not give us any information about the system's forces. Therefore, it is preferable to use a structural form-finding method to understand the behavior of the cellular structures in the design process, while being able to change the topology of the pin-jointed system to result in new structures (section 1.3).

This research proposes a potential application of the geometry-based structural form-finding technique in the context of material science and mechanical engineering. It introduces the geometry-based structural form-finding technique to design cellular materials and shows the relationship between the structure's geometry and flow of force. Moreover, it presents a method to simulate well-known cellular and shellular materials (e.g., Schwartz P, D, and Gyroid) using the geometry-based form-finding technique while controlling the internal force-flow of the structure to achieve different geometrical typologies (i.e., from truss cellulars to shellular materials).

2 METHODOLOGY

As mentioned in section 1.4.2, according to the principles of 3d graphic statics, a closed and convex force diagram in 3D can represent a compression-only or tension-only structural system in equilibrium. In the design process of a cellular material's unit-cell, it is always guaranteed that the force-flow will be in equilibrium if we start from designing a force diagram in 3d, but the other way around is not valid. This is the main advantage of designing a structural system via 3DGS compared to other methods. Besides, since the magnitude of the force in each member in the form diagram is proportional to the area of the corresponding face in the force diagram, by designing the force diagram, we would be aware of the load ratio of the members in the form diagram (Figure 4) [Akbarzadeh et al. 2015a]. Therefore, to design a unit cell of a periodic cellular material (as a form diagram), we start by designing its dual (force diagram). Designing the dual needs understanding the properties of the dual, including the global and nodal equilibrium and the techniques to change the internal equilibrium without disturbing the global equilibrium. In this process, we use PolyFrame

(a) $\mathrm{A}(f^\dagger) = |f_j|$ (e)

(b) $|f_j| = 4 \times |f_{j,1}|$ (f)

(c) $|f_j| = 16 \times |f_{j,2}|$ (g)

(d) $|f_j| = 64 \times |f_{j,3}|$ (h)
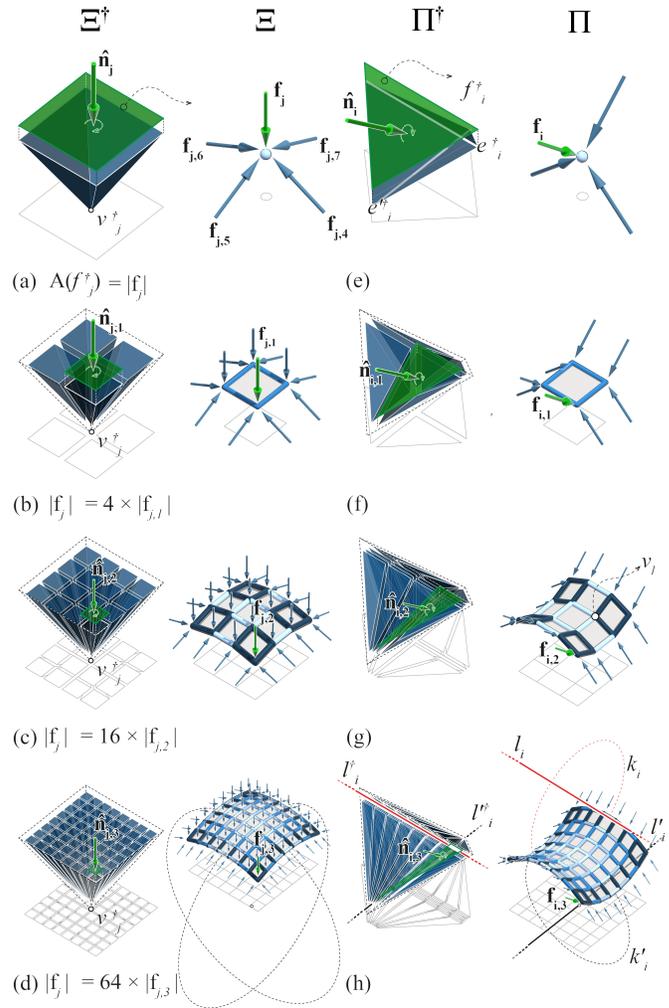
Figure 5: Specific iterative subdivision of the force diagram would result discrete synclastic or anticlastic surfaces; (a-d) the process of subdividing a pyramid as a force diagram to result a synclastic surface as a form diagram; (e-h) the process of subdividing a tetrahedon through two axes (labyrinths) as a force diagram to result a discrete anticlastic surface as a form diagram.

beta [Nejur and Akbarzadeh 2018] plugin for Rhinoceros software [McNeel 2014] to generate the form and the force diagrams.

2.1 Nodal equilibrium in 3DGS

A closed and convex polyhedron represents the equilibrium of a single node (under compression or tension) in 3d (Figure 4a) [Akbarzadeh et al. 2015b; Baumgart 1975]. The force diagram's side faces correspond to the number of forces applied to a node as a form diagram (in Figure 4a, a cube as a force diagram represents a node in equilibrium with six external loads as a form diagram). Each of the six external forces in the form diagram corresponds to an external face (global face) in the force diagram. Therefore,

$\Xi^{\dagger}$

Ξ

$\Pi^{\dagger}$

Π

(a)

$l'^{\dagger}_{i,l} \parallel l'_{i,l} \; , l^{\dagger}_{i,l} \parallel l_{i,l}$

(d)

(b)

$l'^{\dagger}_{j,l} \parallel l'_{j,l} \; , l^{\dagger}_{j,l} \parallel l_{j,l}$

(e)

(c)

$l'^{\dagger}_{k,l} \parallel l'_{k,l} \; l^{\dagger}_{k,l} \parallel l_{k,l}$

(f)
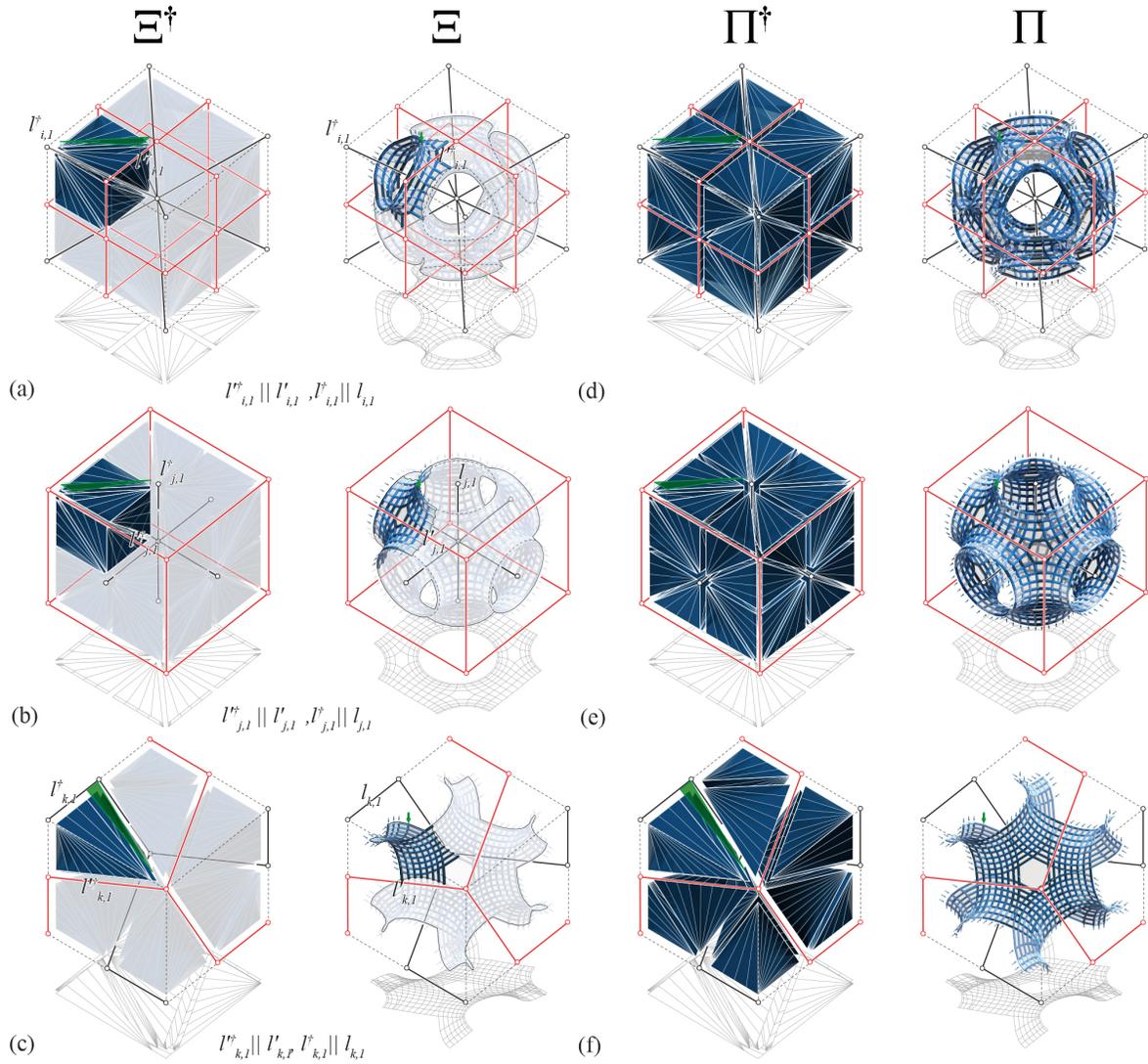
Figure 6: Approximating three unit-cells of well-known minimal surfaces via 3DGS: (a and d) force and diagrams of a discrete unit-cell approximating Schwarz w surface (eightfold-coordinated Schwarz W unit-cell), (b and e) force and form diagrams of a discrete unit cell approximating Schwarz P surface (sixfold-coordinated Shwartz P unit-cell); (c and f) force and form diagrams of a Gyroid's patch approximation (threefold-coordinated, part of a Gyroid unit-cell). Notice that pair of labyrinths for each unit cell have been shown as red and black 3d graphs.

each closed cell in the force diagram corresponds to a single node in the form diagram, satisfying a local equilibrium in the system. Subdividing the force diagram (the cube) to six closed cells (Figure 4b, $\Xi^{\dagger}$) would result a cell with six nodes connected with eight edges as a form diagram (Figure 4b, $\Xi^{\dagger}$). Each of the eight edges in the form diagram corresponds to an internal face (local face) in the force diagram. Also, the node in the center of the subdivided force diagram (Figure 4b) corresponds to a cell in the form diagram. Adding thickness to the edges of the form diagram, proportional to the area of the reciprocal faces in the force diagram, visualizes the magnitude of the forces in the form diagram's edges (Figure 4) [Akbarzadeh et al. 2015b].

2.2 Global equilibrium in 3DGS

In 3d reciprocal form and force diagrams, the global equilibrium of a spatial compression-only form is represented by a convex polyhedron, which provides the magnitude and the direction of the reaction forces at the supports (Figure 4a). The external faces of the force diagram (global faces) correspond to the applied loads and the reaction forces. Regardless of the internal topology of the force-flow in the form diagram (Figure 4a-d), the external forces are in equilibrium if the external faces of the force diagram (corresponding to the applied loads) establish a closed force polyhedron. For instance, in Figure 4a-d, the external faces of the force diagram are fixed as a

cube corresponding to the equilibrium of the six applied loads in the form diagrams.

2.3 Internal equilibrium (Effect of subdivision of the force diagram on the topology of the form diagram)

Subdividing the force diagram's internal space results in a variety of topologically-different structural forms for a given boundary condition and loading scenario [Harboe Nielsen et al. 2017]. There are two main approaches to subdivide a force diagram; We can either subdivide the faces of the global force polyhedron and internal space of the global force polyhedron (Figure 4e-h) or subdivide the internal space of the force diagram without disturbing the global equilibrium of the system (Figure 4a-d). In the first approach, the quantity and magnitude of the reaction forces have been changed. For instance, in Figure 4e-h, by subdividing the internal space and global faces of the force diagram, the form diagram with six reaction forces (Figure 4e) is altered to a form diagram with 48 reaction forces. Therefore, the magnitude of each reaction force is changed from $|f_i|$ to $|f_{i,3}| = |f_i|/8$. While in Figure 4a-d, by subdividing the internal space of the force diagram without changing the global faces, the quantity and magnitude of the reaction forces have not been changed.

2.4 Cellular funicular geometries

To design a unit cell of a periodic truss cellular material, first, the applied loads' location needs to be determined. Then, according to the section 2.2, the global force diagram corresponding to the applied forces should be generated as a closed polyhedron with each face perpendicular to the corresponding applied forces in the form diagram (Figure 4a). Then the force diagram can be subdivided in 3D (see section 2.3) in order to result in a form diagram. Different subdivisions results various form diagrams, enable us to explore a wide range of possibilities (Figure 4 and 5). The resulted form diagram, as a pin-jointed network, only represents the force-flow of a structure. The form diagram is visualized by adding thickness to the links or faces to result in struts or membranes as structural members of the cellular material. As mentioned in sections 1.4.1 and 1.4.2, both reciprocal diagrams consist of vertices, edges, faces, and cells. Therefore, in the visualization process, one can either add thickness to the edges of the form diagram (Figure 8a,b,c) or to the faces between the edges (Figure 8d). In order to design a truss cellular structure, each edge of the form diagram can be translated to a strut member which its thickness is proportional to the area of the corresponding face in the reciprocal force diagram(Figure 4h) [Akbarzadeh et al. 2015b]. The structural performance of truss cellular materials with slender members relies heavily on the *buckling* performance of the system. By increasing the number of subdivisions while keeping the volume constant, we would have shorter edges and distributed external loads in the form diagram (e.g., Figure 4e-h), which would increase the maximum buckling force in the structural system [Harboe Nielsen et al. 2017].

2.5 Shellular funicular geometries

Shellular (shell cellular) systems are the third category of cellular structures discussed in this paper. These structures are ultra-low density materials in nature composed of a single, continuous, smooth-curved shell (Figure 2c) [Han et al. 2015a]. Due to their complex geometry, the modeling process of this type of geometries is a challenging task. In this section, the authors introduce a novel approach for generating these structures in 3DGS. This technique allows us to design shellular materials while understanding the relationship between form and force and modify or optimize the structure's force-flow by changing its reciprocal force diagram. As mentioned in section 2.3 and 2.4, by increasing the number of internal subdivisions in the force diagram, we would have shorter edges and distributed external loads in the form diagram (e.g., Figure 4e-h) In the force diagram, if we repeat specific types of subdivision iteratively, we can shorten the edges of the form diagram until their length gets near to zero (Figure 5d,h). Therefore, with this technique, we can approximate a surface in 3DGS (discrete surface) [Akbari et al. 2019]. There are specific subdivision rules in 3DGS, resulting in a polyhedral surface geometry with synclastic or anticlastic properties. The figure 5a-d shows a subdivision process that translates a single node in equilibrium into a discrete synclastic surface. The global force diagram of a discrete synclastic surface is a pyramid with a square base (Figure 5a), which is reciprocal to a node with five forces in equilibrium as a form diagram. Subdividing the square base (in the force diagram) to four squares and extruding them to the bottom vertex $v_j^\dagger$ would result in a square as a form diagram with eight forces from the sides and four forces from the top (Figure 5b). Similar iterative subdivision results a discrete synclastic surface as a form diagram (Figure 5c,d). Increasing the subdivision number will improve the geometry's resolution as a continuous surface (Figure 5c,d). This iterative subdivision around the vertex $v_j^\dagger$ results in a discrete surface with two principal curvatures. We noticed that the center of curvature of the surface is located on the vertex $v_j^\dagger$, if we relocate the form diagram on top of the force diagram. Therefore, this point can be considered a control point in the force diagram to tune the curvature of the discrete synclastic surface (Figure 5d).

2.5.1 Anticlastic polyhedral geometries in 3DGS. Shellular geometries (e.g., minimal surfaces) consist of an aggregation of anticlastic patches. Therefore, to design a shellular structure, we need to find a way to design an anticlastic surface in 3DGS. As mentioned in section 1.1.3, an anticlastic surface is a surface with centers of curvature on opposing sides. Hence, to design an anticlastic surface, we need two axes of curvatures as two skew lines in R^3 and the surface in between (Figure 5e). As mentioned in section 2.5, the curvature center of a surface can be found in the force diagram of the structure. We used this property to design a global force diagram for an anticlastic surface between two skew lines (Figure 5e). Global force diagram of a discrete anticlastic surface is a tetrahedron corresponding to a node with four external forces in equilibrium (two *hanging* and two *standing*) as the form diagram (Figure 5e). In order to translate this node to a continuous shellular geometry, we need to apply the **anticlastic subdivision technique** to subdivide the force diagram into a group of smaller tetrahedrons. In each step of
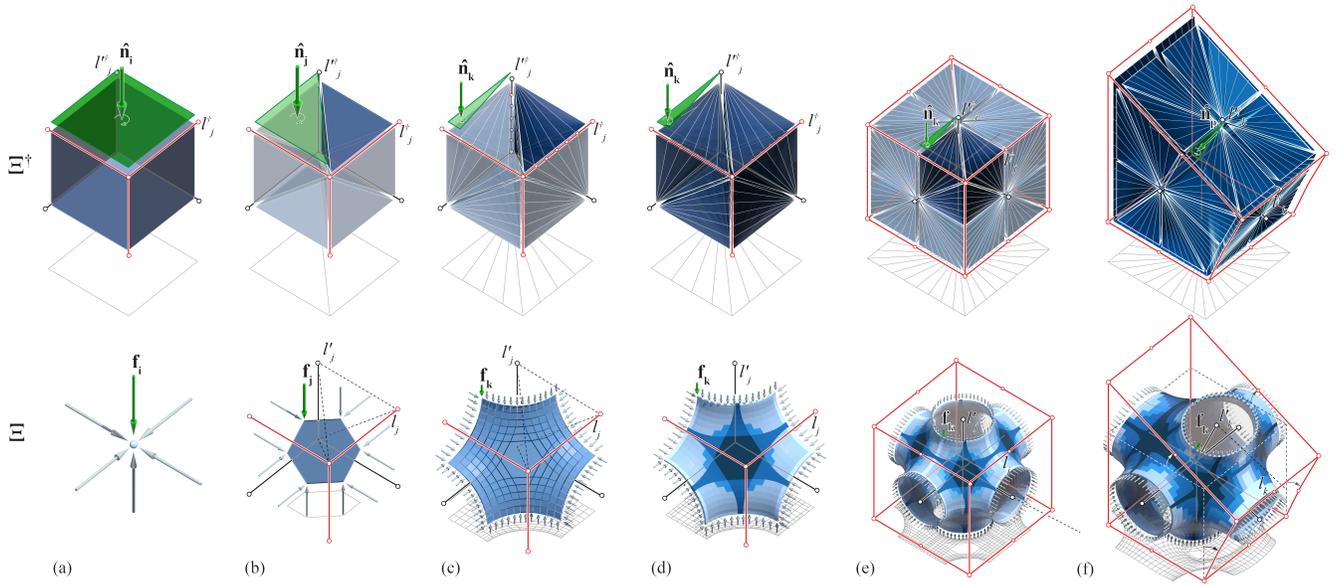
Figure 7: Approximating Schwarz's P surface's unit-cell in 3DGS; (a) A Cube, as the global force diagram. (b) Two sets of labyrinths create six tetrahedrons in between, resulting in a truss-based geometry. (c) Applying the anticlastic subdivision technique. (d) Adding thickness to the surface. (e) Mirroring the surface patch in x, y, and z directions approximate Schwarz's P unit-cell. (f) Changing the labyrinths' geometry results in unit-calls with new geometries.

this technique, two highlighted edges of the global force diagram, $l_i^\dagger$ and $l_i'^\dagger$, are divided into an equal number of segments such that each segment of the former will establish a tetrahedron with its associated segment in the latter (Figure 5f,g). Further subdivisions of those edges will result in a smoother surface as a form diagram (Figure 5h). However, for this subdivision to work, the force diagram cells should only consist of tetrahedrons. This results in each node (e.g. v_l) on the surface (Figure 5f) to be connected only to four other nodes with two *hanging* edges and two *standing* edges which establishes the negative Gaussian curvature (Figure 5f,g). Moreover, the resulting anticlastic surface of Figure 5 in the form diagram is only subjected to the applied loads from sides with no load applied to the nodes on the surface. As shown in Figure 5h, the curvature axes in an anticlastic surface (l_i and l_i') is subdivision axes in the reciprocal force diagram ($l_i^\dagger$ and $l_i'^\dagger$).

2.5.2 *The role of labyrinths in designing anticlastic polyhedral geometries in 3DGS .*
Anticlastic surface geometries in 3DGS (similar to minimal surfaces) subdivide R^3 into two segregated regions, each of which is connected in space and forms a 3D connectivity graph named *labyrinth* (Figure 6a,b,c) [Fischer and Koch 1989, 1990]. Two labyrinths interpenetrate each other with the surface as their common interface. The geometry of the surface changes when the angle of these labyrinths changes [Fischer and Koch 1989]. Figure 5h shows two skew labyrinths of l_i and l_i' shape an anticlastic surface in between. In this technique, in a force diagram, the angle between the axes (labyrinths) can change the diagram's geometry. According to Figure 5f , if we consider l_i and l_i' as the labyrinths of the anticlastic surface , we observe that they play

the role of subdivision axes in the force diagram ($e_i^\dagger || l_i$ and $e_{i'}^\dagger || l_i'$) and the role of labyrinths and the surface's curvature axes in the form diagram (Figure 5h). For a specific type of anticlastic surface, we can identify the topology of a specific surface with anticlastic curvature based on the geometry of its labyrinths. [Fischer and Koch 1989] Since the same labyrinths play the role of subdivision axes in the force diagram of the anticlastic surface, we may use them as common geometrical elements between the force and the form diagram of a structure. In this technique, We can use these labyrinths as control handles in the force diagram to design the form diagram. This technique enables us to design compression-only or tension-only unit-cells of shellular materials by designing their labyrinths' network.

2.5.3 *Designing an anticlastic surface unit-cell in 3DGS .*
To design a periodic shellular material in 3DGS, we can start with designing a periodic unit-cell and then try to aggregate it in three directions. The main steps for designing a unit-cell of Schwarz's P surface in 3DGS are explained below (Figure 7). In each step, the force diagram is designed in the Rhinoceros software's environment, [McNeel 2014], and the form diagram is created using the PolyFrame-beta plugin. [Nejur and Akbarzadeh 2018]

(1) A global force diagram's geometry is defined based on the external loading scenario. To design a triply periodic cellular material, a cube is considered as the global force diagram to aggregate in three directions (Figure 7a).

(2) The next step is to design the geometry of the unit-cells' labyrinths. According to the literature, Schwarz's P surface's labyrinths consist of two sets of 3D graphs, one as a cubic wire-frame with 12 edges and the other as 6 intersecting
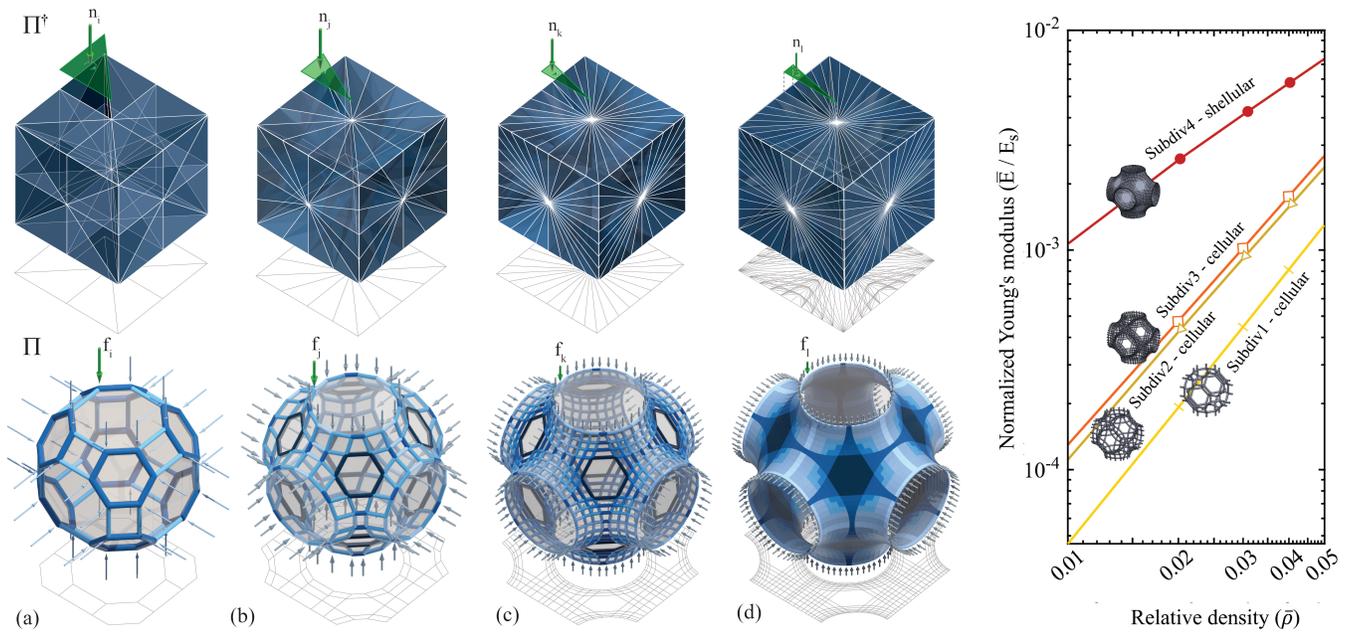
Figure 8: Left : four different pairs of reciprocal diagrams with different degrees of subdivision simulating a Schwarz P unit-cell with different resolution (from a truss-based cellular geometry (a) to a shell-based cellular or shellular geometry (d)). Right : comparison of normalized Young modulus for cellular materials with different subdivisions in 5 different relative densities.

edges perpendicular to each other (Figure 6b). [Schoen 1970; Schwarz 1890]

(3) Since the geometry of the Schwarz's P unit-cell has reflectional symmetry in three main axes (x, y, and z), the design process can be simplified by designing 1/8 section of the unit-cell. Accordingly, 1/8 of the labyrinths' geometry leaves us with two labyrinths' sets, each of which consists of three edges perpendicular to each other (Figure 7a, b). Each line from one set neither intersect nor is parallel to a line in the second set. These lines define three pairs of *skew lines* (e.g., $l_i^\dagger$ and $l_i'^\dagger$).

(4) In order to create a force diagram based on the labyrinths' sets, the labyrinths' 3D graph is translated to a group closed polyhedron geometries. As mentioned in section 2.5.1, a specific aggregation of tetrahedrons as a force diagram results in a discrete anticlastic surface as a form diagram. Here, each line from the first set produces two tetrahedrons with corresponding skew lines in the second set, resulting in six tetrahedrons (Figure 7b).

(5) The form diagram of the designed force diagram is a truss cellular geometry with extended members (Figure 7b). This structural form has polyhedral configurations, including vertices, edges, faces, and cells. In order to translate this geometry to a continuous surface-based geometry, each tetrahedron needs to be subdivided with the anticlastic subdivision technique described in section 2.5.1 (Figure 7c). Increasing the number of subdivisions in the force diagram results in smaller edges in the form diagram. Applying the anticlastic subdivision technique (by dividing each labyrinth's edge

to 6 segments) subdivides each tetrahedron to 36 tetrahedrons, replacing each node in the previous form diagram to a network of 36 nodes. Presenting this structural form as a group of connected faces approximates an anticlastic surface (a patch of Schwarz P surface) in equilibrium for a specific boundary condition.

(6) Adding thickness to the discrete surface can create a shell, resulting in a shellular material (Figure 7d). According to the principles of 3DGS, the magnitude of the force in the form diagram's member is proportional to the corresponding face's area in the force diagram. In this technique, each group of four intersecting faces in the force diagram corresponds to a group of closed edges in the form diagram. Consequently, each face's thickness in the form diagram is proportional to the corresponding faces' total area in the force diagram. Therefore, to have constant stress along the surface, the surface needs to be materialized with a variable offset. In Figure 7d, the faces with darker color have a greater thickness than the others.

(7) Mirroring the geometry of the form diagram in 3 directions results in an approximation of the Schwarz P's unit-cell (Figure 7e).

(8) Changing the labyrinths' geometry results in a new type of anticlastic polyhedral surface, designed for a new boundary condition (Figure 7f).

2.5.4 Generating well-known anticlastic surface geometries using 3DGS. Similarly, we can explore different anticlastic patches' aggregations to achieve well-known anticlastic surfaces' typologies

based on their labyrinths' geometry. We created three types of anticlastic surface unit cells resembling well-known minimal surfaces such as Gyroid(G), Schwarz Primitive(P), and Schwarz iWp(W) (Figure 6). For each surface, for a certain boundary condition in the force diagram (the cube), the anticlastic surface's labyrinths have been located in the global force, and each two skew lines from each group of labyrinths have been connected together with a tetrahedron (Figure 6a,b,c). These tetrahedrons have been subdivided in order to increase the resolution of the anticlastic surface as the form diagram (Figure 6). Different geometries of the labyrinths in the force diagram result in new surfaces as the form diagram. For instance, in the process of modeling the resembling unit-cell of Schwarz iwp(w) (Figure 6a), $l_{i,1}^{\dagger}$ and $l_{i,1}'^{\dagger}$ are in 54.7 degree angle while $l_{j,1}^{\dagger}$ and $l_{j,1}'^{\dagger}$ in Schwarz P (Figure 6b) are in 90 degree angle and $l_{k,1}^{\dagger}$ and $l_{k,1}'^{\dagger}$ in Gyroid (Figure 6c) are in 60 degree angle. Besides, different aggregations of the patches for each surface in the form diagram (which corresponds to its reciprocal tetrahedron in the force diagram) can result new types of geometry. Although these structures follow the geometry of well-known minimal surfaces, we can name them minimal surfaces if and only if they are continuous anticlastic surfaces with *zero mean curvature* [Schoen 1970].

2.6 Aggregation of cellular units

Suppose we consider each of the form diagrams in Figure 6d,e,f as a unit cell of a larger system (e.g., a cellular material), by aggregating the force diagrams and constructing the reciprocal form diagram. In that case, we can result in a compression-only (or tension-only) shell cellular material (Figure 1b). The same process can be applied to the truss-based unit-cells (Figure 1a). Different types of aggregation can result in new geometries (e.g., mirroring the resembling of the gyroid unit-cell instead of copying in X, Y, and Z directions). Furthermore, deforming different parts of the aggregated force diagram results in a non-homogeneous structure with variable unit cells in each part.

2.7 Analytical studies

2.7.1 From a truss-cellular unit cell towards Schawrz P surface. As shown in Figure 5(e-h), increasing the number of subdivisions in this technique would increase the resolution of the final anticlastic surface to get closer to a continuous surface. Similarly, for resembling a unit-cell of a Schwarz P surface (Figure 8), increasing the number of subdivisions would change the resolution of the geometry and gradually change its character from a truss cellular geometry towards a shell-based cellular (shellular) geometry.

2.7.2 Effect of anticlastic subdivision on mechanical performance of the cellular materials. Finally, We compare the structural performance of four periodic cellular materials with unit cells resembling Primitive TPMS. These unit cells have been generated in 3DGS with the same labyrinths but different degrees of subdivision (see section 2.5.4). To investigate mechanical properties of cellular materials made out of the designed architectures, standard mechanics homogenization is applied on their unit cells under periodic boundary conditions [Hollister and Kikuchi 1992], and their effective Young's and shear moduli ($\bar{E}$ and $\bar{G}$ respectively), together with their effective Poisson's ratios ($\bar{E}$) are numerically obtained using ANSYS APDL.

A family of architectures, resembling Primitive TPMS, is selected to showcase the effect of refining the architecture by increasing the number of subdivisions in the force diagram and comparing the mechanical performances of the truss cellular materials with their shellular counterpart at relative densities from 1 to 5 percent. Considering the existing symmetries in these architectures (which result in their orthotropic properties), it is enough to report their effective mechanical properties along with one of the coordinate axes only. As shown in Figure 8, refinement of the lattice architectures brings the effective Young's moduli $\bar{E}$ closer to those of the shellular case. The initial considerable difference between the moduli of the truss cellular and the shellular materials is attributed to the fact that these truss architectures are originally designed for triaxial loading, and the ideal design consists of two force members with frictionless joints, which under the uniaxial or shear loadings, make them mechanisms with non-zero static and kinetic degrees of freedom. On the other hand, for the cellular materials at small relative densities, small joints and slender links make them behave more like a mechanism rather than a solid material. Therefore, under uniaxial or shear loading, the shellular counterpart exhibits significantly stiffer load-displacement performance. It is worth noting that because of the specific method that is used for making the subdivisions, mechanical properties of the discussed family of the lattice materials will not reach to those of the shellular counterpart, which provides a wider range of effective mechanical properties and potentially attracts different applications compared to the shellular analogue.

3 CONCLUSION AND FUTURE WORKS

Three-dimensional graphic statics (3DGS) as a geometry-based structural form-finding method can design a variety of cellular materials with different geometries in 3D. This paper showed that 3DGS enables us to design infinite efficient light-weight cellular materials for different boundary conditions with various internal topology and force distribution. In this system, the resulted geometry depends on the external force polyhedron, force diagram's internal subdivision, and geometrical degree of freedom of the pin-jointed system [Hablicsek et al. 2018]). This method lets us understand the relationship between the internal flow of force, geometry, and external force-flow with their geometrical relationships. Besides, by designing a structure's force diagram, we always guarantee that the force-flow will be in equilibrium. Moreover, We introduced a novel form-finding method in 3DGS to design shell cellular (shellular) geometries with different levels of subdivision based on designing two sets of labyrinths. These labyrinths would facilitate the design process of shellular geometries and let us design and control the structure's geometry without concerning about the 3d subdivision of the force diagram. Many aspects of the proposed methodology require further exploration to establish a complete form-finding method for cellular materials. Such explorations could be concerned with designing cellular materials for a specific boundary condition, effect of changing the geometry of the labyrinths in curvature, force-flow and structural capacity of the shellular funicular material, to name but two.

REFERENCES

Sigrid Adriaenssens, Philipe Block, Diederik Veenendaal, and Chris Williams. 2014. *Shell structures for architecture, form finding and optimization.* Routledge.

M. Akbari, M. Akbarzadeh, and M. Bolhassani. 2019. From Polyhedral to Anticlastic Funicular Spatial Structures. In *Proceedings of IASS Symposium 2019 and Structural Membranes 2019, FORM and FORCE.* Barcelona, Spain.

M Akbarzadeh. 2016. *3D Graphical Statics Using Reciprocal Polyhedral Diagrams.* Ph.D. Dissertation. ETH Zruich, Stefano Franscini Platz 5, Zurich, CH, 8093.

M Akbarzadeh, T Van Mele, and P Block. 2015a. 3D Graphic Statics: Geometric Construction of Global Equilibrium. In *Future Visions.* Proceedings of the International Association for Shell and Spatial Structures (IASS) Symposium 2015.

M Akbarzadeh, T Van Mele, and P Block. 2015b. On the equilibrium of funicular polyhedral frames and convex polyhedral force diagrams. *Computer-Aided Design* 63 (2015), 118–128.

M Akbarzadeh, T Van Mele, and P Block. 2016. Three-dimensional graphic statics: Initial explorations with polyhedral form and force diagrams. *International Journal of Space Structures* 1 (2016).

Bruce G Baumgart. 1975. A polyhedron representation for computer vision. In *Proceedings of the May 19-22, 1975, national computer conference and exposition.* 589–596.

Martin Philip Bendsoe and Noboru Kikuchi. 1988. Generating optimal topologies in structural design using a homogenization method. (1988).

Dhruv Bhate, Clint A Penick, Lara A Ferry, and Christine Lee. 2019. Classification and selection of cellular materials in mechanical design: Engineering and biomimetic approaches. *Designs* 3, 1 (2019), 19.

Philippe Philippe Camille Vincent Block. 2009. *Thrust network analysis: exploring three-dimensional equilibrium.* Ph.D. Dissertation. Massachusetts Institute of Technology.

Jules Bloomenthal and Keith Ferguson. 1995. Polygonization of non-manifold implicit surfaces. In *Proceedings of the 22nd annual conference on Computer graphics and interactive techniques.* 309–316.

RM Christensen. 1986. Mechanics of low density materials. *Journal of the Mechanics and Physics of Solids* 34, 6 (1986), 563–578.

Luigi Cremona. 1890. *Graphical Statics: Two Treatises on the Graphical Calculus and Reciprocal Figures in Graphical Statics...* Claredon Press.

Carl Culmann. 1864. Bericht an den hohen schweizerischen Bundesrath über die Untersuchung der schweiz. *Wildbäche, vorgenommen in den Jahren 1858, 1859, 1860 und 1863* (1864).

VS Deshpande, MF Ashby, and NA Fleck. 2001. Foam topology: bending versus stretching dominated architectures. *Acta materialia* 49, 6 (2001), 1035–1040.

M.P. do Carmo. 1976. *Differential Geometry of Curves and Surfaces.* Prentice-Hall, Engelwood Cliffs, NJ.

M Eynbeygui, J Arghavani, AH Akbarzadeh, and R Naghdabadi. 2020. Anisotropic elastic-plastic behavior of architected pyramidal lattice materials. *Acta Materialia* 183 (2020), 118–136.

W. Fischer and E. Koch. 1989. Genera of minimal balance surfaces. *Acta Crystallographica Section A* 45, 10 (1989), 726–732. https://doi.org/10.1107/S0108767389006616 arXiv:https://onlinelibrary.wiley.com/doi/pdf/10.1107/S0108767389006616

W Fischer and E Koch. 1990. Crystallographic aspects of minimal surfaces. *Le Journal de Physique Colloques* 51, C7 (1990), C7–131.

Lorna J Gibson and Michael F Ashby. 1999. *Cellular solids: structure and properties.* Cambridge university press.

Nicholas Goldsmith. 2016. The physical modeling legacy of Frei Otto. *International Journal of Space Structures* 31, 1 (2016), 25–30.

M. Hablicsek, M. Akbarzadeh, and Y. Guo. 2018. Algebraic 3D graphic statics: Reciprocal constructions. *Computer-Aided Design* (2018).

Seung Chul Han, Jeong Myung Choi, Gang Liu, and Kiju Kang. 2017. A Microscopic Shell Structure with Schwarz's D-Surface. *Scientific Reports* 7, 1 (2017), 13405.

Seung Chul Han, Jeong Woo Lee, and Kiju Kang. 2015a. A new type of low density material: Shellular. *Advanced Materials* 27, 37 (2015), 5506–5511.

Seung Chul Han, Jeong Woo Lee, and Kiju Kang. 2015b. A New Type of Low Density Material: Shellular. *Advanced Materials* 27, 37 (2015), 5506–5511. https://doi.org/10.1002/adma.201501546 arXiv:https://onlinelibrary.wiley.com/doi/pdf/10.1002/adma.201501546

T Harboe Nielsen, M Akbarzadeh, and P Goltermann. 2017. Addressing buckling of compression members using subdivision of force diagrams. In *Proceedings of the IASS Annual Symposium 2017, Interfaces: architecture . engineering . science.* IASS.

Scott J Hollister and Noboru Kikuchi. 1992. A comparison of homogenization and standard mechanics analyses for periodic porous composites. *Computational Mechanics* 10, 2 (1992), 73–95.

X Huang, SW Zhou, YM Xie, and Q Li. 2013. Topology optimization of microstructures of cellular materials and composites for macrostructures. *Computational Materials Science* 67 (2013), 397–407.

Stephen Hyde, Z Blum, T Landh, S Lidin, BW Ninham, S Andersson, and K Larsson. 1996. *The language of shape: the role of curvature in condensed matter: physics, chemistry and biology.* Elsevier.

Victor J Katz. 1979. The history of Stokes' theorem. *Mathematics Magazine* 52, 3 (1979), 146–156.

Min Lai, Alex N Kulak, Daniel Law, Zhibing Zhang, Fiona C Meldrum, and D Jason Riley. 2007. Profiting from nature: macroporous copper with superior mechanical properties. *Chemical communications* 34 (2007), 3547–3549.

Hang-Shing Ma, Jean-H Prévost, Rémi Jullien, and George W Scherer. 2001. Computer simulation of mechanical structure–property relationship of aerogels. *Journal of non-crystalline solids* 285, 1-3 (2001), 216–221.

J Clerk Maxwell. 1864. L. on the calculation of the equilibrium and stiffness of frames. *The London, Edinburgh, and Dublin Philosophical Magazine and Journal of Science* 27, 182 (1864), 294–299.

R McNeel. 2014. Rhinoceros: NURBS modeling for Windows. Computer software. http://www.rhino3d.com/

Lucas R Meza, Satyajit Das, and Julia R Greer. 2014. Strong, lightweight, and recoverable three-dimensional ceramic nanolattices. *Science* 345, 6202 (2014), 1322–1326.

A Nejur and M Akbarzadeh. 2018. PolyFrame beta: a geometry-based structural form finding plugin for Rhinoceros3d. https://www.food4rhino.com/app/polyframe.

Ulrich Pinkall and Konrad Polthier. 1993. Computing discrete minimal surfaces and their conjugates. *Experimental mathematics* 2, 1 (1993), 15–36.

Zhao Qin, Gang Seob Jung, Min Jeong Kang, and Markus J. Buehler. 2017. The mechanics and design of a lightweight three-dimensional graphene assembly. *Science Advances* 3 (01 2017), e1601536. https://doi.org/10.1126/sciadv.1601536

Srinivasan Rajagopalan and Richard A Robb. 2006a. Schwarz meets Schwann: design and fabrication of biomorphic and durataxic tissue engineering scaffolds. *Medical image analysis* 10, 5 (2006), 693–712.

Srinivasan Rajagopalan and Richard A Robb. 2006b. Schwarz meets Schwann: design and fabrication of biomorphic and durataxic tissue engineering scaffolds. *Medical image analysis* 10, 5 (2006), 693–712.

WJ Macquorn Rankine. 1864. XVII. Principle of the equilibrium of polyhedral frames. *The London, Edinburgh, and Dublin Philosophical Magazine and Journal of Science* 27, 180 (1864), 92–92.

Aristides AG Requicha and Herbert B Voelcker. 1977. Constructive solid geometry. (1977).

Gianpaolo Savio, Stefano Rosso, Roberto Meneghello, and Gianmaria Concheri. 2018. Geometric modeling of cellular materials for additive manufacturing in biomedical field: a review. *Applied bionics and biomechanics* 2018 (2018).

Eike Schling, Denis Hitrec, and Rainer Barthel. 2017. Designing Grid Structures Using Asymptotic Curve Networks. 125–140. https://doi.org/10.1007/978-981-10-6611-5_12

Alan H. Schoen. 1970. *Infinite Periodic Minimal Surfaces without Self-intersection.* NASA.

Hermann Amandus Schwarz. 1890. *Gesammelte mathematische abhandlungen.* Vol. 1. J. Springer.

J Shi and AH Akbarzadeh. 2019. Architected cellular piezoelectric metamaterials: Thermo-electro-mechanical properties. *Acta Materialia* 163 (2019), 91–121.

Ole Sigmund and Kurt Maute. 2013. Topology optimization approaches: A comparative review, 2013. *ISSN 1615147X* (2013).

Jean-Marc Thiery, Bert Buchholz, Julien Tierny, and Tamy Boubekeur. 2012. Analytic curve skeletons for 3d surface modeling and processing. In *Computer Graphics Forum*, Vol. 31. Wiley Online Library, 2223–2232.

A Torrents, TA Schaedler, AJ Jacobsen, WB Carter, and L Valdevit. 2012. Characterization of nickel-based microlattice materials with structural hierarchy from the nanometer to the millimeter scale. *Acta Materialia* 60, 8 (2012), 3511–3523.

Tom Van Mele, Lorenz Lachauer, Matthias Rippmann, and Philippe Block. 2012. Geometry-based understanding of structures. *Journal of the international association for shell and spatial structures* 53, 4 (2012), 285–295.

Diederik Veenendaal and Philippe Block. 2012. An overview and comparison of structural form finding methods for general networks. *International Journal of Solids and Structures* 49, 26 (2012), 3741–3753.

William Sidney Wolfe. 1921. *Graphical analysis: a text book on graphic statics.* McGraw-Hill book Company, Incorporated.